Available online at www.sciencedirect.com

ScienceDirect

journal homepage: www.elsevier.com/locate/he

The influence of gaseous hydrogen charging on the microstructural and mechanical behavior of electron beam melted and wrought Ti–6Al–4V alloys using the small punch test

Noa Lulu-Bitton [a,b], Nissim U. Navi [b,**], Brian A. Rosen [a], Shlomo Haroush [b], Eyal Sabatani [b], Yizhaq Eretz-Kdosha [b], Gennadi Agronov [b], Noam Eliaz [a,*]

[a] Department of Materials Science and Engineering, Tel-Aviv University, Ramat Aviv, Tel Aviv, 6997801, Israel
[b] Nuclear Research Center Negev (NRCN), P.O. Box 9001, Beer Sheva, 84190, Israel

HIGHLIGHTS

- The effects of gaseous hydrogenation on EBM and wrought Ti–6Al–4V were compared.
- Both alloys had a similar phase and impurities content in the non-hydrogenated form.
- Both alloys showed a similar mechanical behavior at any hydrogen content.
- Above the β_H saturation point, the mechanical properties degraded significantly.
- Hydrogen-induced degradation is different after gaseous vs. electrochemical charging.

GRAPHICAL ABSTRACT

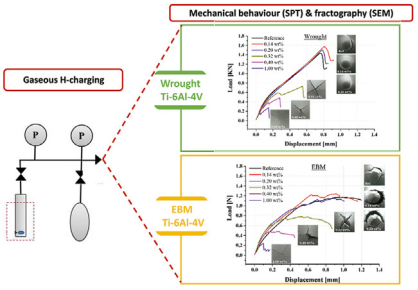

ARTICLE INFO

Article history:
Received 5 April 2023
Received in revised form
8 May 2023
Accepted 14 May 2023
Available online 3 June 2023

ABSTRACT

The influence of gaseous hydrogen charging at 600 °C on the microstructure and mechanical behavior of wrought and Electron Beam Melted (EBM) Ti–6Al–4V alloys was investigated for hydrogen contents between 0.14 and 1.0 wt%. The small punch test (SPT) technique was used to characterize the mechanical behavior of all specimens. Both EBM and wrought alloys containing ~6 wt% β and similar impurity levels showed similar phase content and mechanical property changes at all hydrogen contents, regardless of their original microstructural differences. This similarity can be explained by the high hydrogen diffusivity at the high temperature at which gaseous charging was carried out, and is in

* *Corresponding author.*
** *Corresponding author.*
E-mail addresses: NissimN@nrcn.gov.il (N.U. Navi), neliaz@tauex.tau.ac.il (N. Eliaz).
https://doi.org/10.1016/j.ijhydene.2023.05.141

Keywords:
Additive manufacturing (AM)
Electron beam melting (EBM)
Ti–6Al–4V alloy
Hydrogen embrittlement (HE)
Gaseous hydrogen charging
Small punch test (SPT)

contrast to previous reports where EBM Ti–6Al–4V was found to be more sensitive to hydrogen embrittlement due to low-temperature electrochemical charging. After hydrogenation, α_H and β_H solid solutions were formed. The quantity of the α_H phase reduced gradually with hydrogen content, while forming β_H, α_2, and hydrides. It was found that β_H saturated at 0.27 wt% hydrogen content. Both alloys demonstrated relatively high strength and ductility up to hydrogen content of 0.2 wt%, i.e. below the β_H saturation concentration. Above the β_H saturation concentration, the mechanical properties of the maximum load (P_{max}), deflection at maximum load (δ_{max}), and absorbed energy (E), degraded significantly due to hydride formation.

Introduction

Ti alloys, and especially the dual phase (α+β) Ti–6Al–4V, are used extensively in aerospace applications mainly due to their superior specific strength. They are also utilized in medical applications such as bone implants due to their corrosion resistance in the human body environment [1–3]. The alloy's microstructure at room temperature (RT) contains two phases (α+β); the α phase has an hcp crystal structure, while the β phase has a bcc structure. Aluminum stabilizes the α phase, while vanadium stabilizes the β phase [4]. Mechanical properties and corrosion resistance are highly affected by the alloy microstructure; therefore, it is important to tailor the alloy's microstructure to the desired mechanical properties and/or corrosion resistance. The microstructure can be controlled by different thermo-mechanical processes; therefore, the desired microstructure can be obtained by a combination of specific annealing temperature, cooling rate, and final aging temperature [5]. Various microstructures, including lamellar, equiaxed, and bimodal microstructures, may form during these processes. The influence of the α and β phase content and morphology in Ti–6Al–4V alloy, produced by traditional techniques, on its mechanical properties and corrosion resistance was studied intensively in Refs. [6–10].

It is well known that hydrogen causes hydrogen embrittlement (HE) of the Ti–6Al–4V alloy due to hydride formation [11,12]. The common titanium hydride phases are δ (fcc), ε (fct, $c/a < 1$), and γ (fct, $c/a > 1$) [13–17]. The Ti alloy's sensitivity to hydrogen can be affected by several parameters such as charging conditions and microstructure [18–22]. Regarding microstructure, the sensitivity to hydrogen is also affected by microstructural differences such as the α and β phase content and density of α/β interphase boundaries, since β (bcc) has higher diffusivity and solubility of hydrogen than α (hcp) [13–15,23,24]. Kim et al. [25–27] described the mechanism of hydride nucleation and growth at α/β interphases. In the case of solid solution of hydrogen in Ti alloys, the failure mechanism is different, and may be connected to high strains that evolve in the matrix as a result of the difference in coefficient of thermal expansion (CTE) between the α and β phases [13]. In addition, the β transition temperature decreases rapidly with an increase in the hydrogen content, and hence the volume fraction of the β phase in the α + β phase range increases [28]. Thus, dual-phase alloys with a higher β phase concentration may be less sensitive to hydrogen because hydrogen is more soluble in the β phase compared to the α phase. As a result, for a given hydrogen content, the hydride phase content will be smaller.

Additive manufacturing (AM) processes have several advantages compared to traditional ones, e.g., casting, rolling, extrusion, etc.; these include production of complex components, raw material saving, near-net-shape manufacturing, tailor-made design, etc. Therefore, engineers and industries are motivated to use AM processes for special applications [29,30]. The most common metal AM processes to date are Powder Bed Fusion (PBF), including Electron Beam Melting (EBM) and Selective Laser Melting (SLM), and Directed Energy Deposition (DED) [31,32]. Mechanical properties of EBM and SLM, as-built, heat treated, and after hot isostatic pressing (HIP) was reviewed by Lewandowski and Seifi [33]. It was reported that all tensile properties of AM'ed materials were equal to or higher than (yield and ultimate tensile stressed) than those of forged, wrought, or annealed alloys, while the elongation was lower. Tevet et al. [34] showed that the elastic properties depend on the manufacturing process and on the AM build direction.

Alloys produced by AM techniques have different microstructures compared to wrought alloys. Therefore, it could be expected that such alloys will have different susceptibility to HE. Yet, literature survey reveals that only few studies have been carried out on hydrogen interaction with AM'ed Ti–6Al–4V alloy [15,17–22,24,35–39].

There are two common methods to add hydrogen to titanium alloys: (i) electrochemical charging (EC), which creates hydrogen via cathodic charging at a specimen's surface and is associated with strong hydrogen fugacity [11,18,20,22,38,40–42] which will not be reviewed in this paper, and (ii) gaseous charging (GC, low fugacity), which exposes the sample to gaseous hydrogen pressure, typically at elevated temperatures [15,17,21,24,35,39].

For GC, Silverstein et al. [17] demonstrated that the build direction of SLM Ti–6Al–4V alloy had a substantial impact on the sensitivity to HE. Metalnikov et al. [19] investigated the influence of EC and GC on EBM Ti–6Al–4V alloy compared to the wrought alloy. They reported that hydrides were formed after either EC (γ-TiH and δ-TiH_x) or GC (δ-TiH_x), yet, no cracks were observed on the EBM samples after hydrogenation. In contrast, hydrogenation of wrought Ti–6Al–4V led to significant cracking. Pushilina et al. [24,35] showed that hydrogen sorption kinetics at 500 °C was sensitive to the manufacturing parameters. They reported [24] that a sample with coarser

microstructure had a lower sorption rate at 500 °C, while the sorption kinetics difference at 650 °C was insignificant.

Pushilina et al. [15] investigated phase transitions and microstructure evolution in EBM Ti–6Al–4V alloy due to GC at 650 °C. The volume content of the β phase was ~4%. It was found that the intermetallic Ti_3Al (α_2) phase was produced due to Al enrichment of the primary α phase when hydrogen content increased to 0.29 wt%. In addition, the phase dimensions and volume fraction increased significantly with hydrogen content up to 0.58 wt%, along with precipitation of nano-sized crystals of titanium δ-hydrides. No hydrides were detected during the Ti_3Al formation. This finding indicates that hydrogen atoms are mostly dissolved in the β phase and partially in the Ti_3Al phase. Pushilina et al. [35] also reported that post HT of EBM Ti–6Al–4V at 750 °C for 1 h in vacuum led to a decrease in the hydrogen sorption rate, which they attributed to the lower density of grain boundaries after HT. Laptev et al. [21] investigated the influence of GC on defect structure, hardness, and wear resistance of EBM Ti–6Al–4V. They discovered that when the alloy was hydrogenated to a content of 470 ppm hydrogen, the γ titanium hydride was formed with a volume content of 2.2%. However, when the hydrogen content was increased to 900 ppm, the fraction volume of both the γ hydride and the β phase decreased, and the δ hydride phase was observed. Furthermore, it was found that hydrogen increased the hardness, decreased the wear resistance, and increased the defect concentration. Gaddam et al. [37] examined how the presence of hydrogen affected the tensile and low cycle fatigue (LCF) characteristics of cast and EBM Ti–6Al–4V alloys. The EBM alloy showed higher tensile strength as well as LCF properties compared to the cast alloy, both in hydrogen and in air environments. The fatigue crack growth (FCG) behavior of EBM and wrought Ti–6Al–4V alloys after exposure to a hydrogen environment at high pressure was investigated by Neikter et al. [43]. The EBM alloy was found to have lower resistance to FCG compared to the wrought alloy. Based on our literature survey, only a few studies have been carried out on the influence of GC at high temperature on the mechanical behavior of AM'ed Ti–6Al–4V.

The quasi-static mechanical properties of Ti-based alloys have been measured mainly by traditional techniques such as tensile and compression bending, although new techniques have been developed during the last four decades (since the 1980's), e.g. the small punch test (SPT). This technique was specifically developed for characterization of the mechanical behavior of structural materials in the nuclear industry using small or thin specimens [44]. The typical load-displacement curve for ductile materials exhibits continuous behavior [45], while the curve for semi-brittle and brittle materials exhibits discontinuous load drops ("*pop-in*" phenomenon) and subsequent increase of the load caused by crack initiation and subsequent crack arrest, as described by Altstadt et al. [46]. On the other hand, if a significant load drop (to zero) occurs, it is an indication of crack propagation to total failure. The top view fracture morphology of ductile materials is semicircular in shape, while in semi-brittle or brittle materials it is "*star-like*" [47]. This type of fracture was observed in different alloys and was reported by several researchers. Arroyo et al. [47] studied the rate effect on fracture toughness of CrNiMn alloys in a hydrogen environment. Eliaz et al. [48] studied amorphous FeSiB alloys, whereas Lulu-Bitton et al. [22] studied EC in the EBM Ti–6Al–4V alloy. Owing to the advantages provided by SPT, particularly due to its high sensitivity to changes in the mechanical behavior and the mode of fracture following hydrogen charging, researchers adapted this technique to investigate the influence of hydrogen on the mechanical behavior of steels [49–53]. It was reported that this technique exhibits exceptional sensitivity to the changes in mechanical behavior and fracture mode due to different hydrogen charging conditions.

Studies of the mechanical behavior of AM'ed Ti–6Al–4V alloy by means of the SPT method are rare. Lucon et al. [54] investigated the mechanical properties of EBM Ti–6Al–4V in different metallurgical conditions, including the as-built condition and after a variety of heat treatments and HIP. It was reported that the SPT curves of the AM'ed alloy contained one or more load drops ("*pop-in*") before or after the recorded maximum load. Additionally, it was discovered that there was very low empirical correlation between the small punch parameters and the tensile mechanical properties (yield and ultimate stresses, strain, etc.). Illsley et al. [55] used the SPT to characterize the mechanical behavior of EBM Ti–6Al–4V at RT. They reported that the ductility at RT was lower than that of cast, HIPed, and forged alloys (but, phase compositions were not recorded). A mix-mode fracture was observed as shown by a fracture consisting of radial cracks with "*star-like*" appearance.

In our previous study [18,22], it was reported that the EBM alloy was more susceptible to HE following EC than a wrought alloy. Higher mechanical degradation of EBM alloy was accompanied by significant fracture mode changes following exposure of wrought and EBM alloys to hydrogen [22]. This was explained by the evolution of a surface hydride layer with a higher concentration of δ_a and δ_b hydrides (variants of δ (TiH_x) having fcc unit cell with space group $Fm\bar{3}m(225)$ [18]) in the wrought alloy. These hydrides served as a barrier for hydrogen uptake into the bulk, and therefore increased the resistance of the wrought alloy to HE by comparison to the EBM alloy.

The goal of the current study is to explore the influence of the type of hydrogen charging (EC & GC) on the microstructure and mechanical behavior of EBM and wrought TI-6Al–4V alloy. The influence of dissolved hydrogen and hydrides following gaseous charging at 600 °C on the microstructure and mechanical behavior of EBM Ti–6Al–4V alloy compared to its counterpart wrought alloy was investigated. To the best of our knowledge, such a comprehensive study that compares the influence of high-temperature GC on the microstructure and mechanical properties of EBM and wrought Ti–6Al–4V alloys with a similar α+β phase content and impurity levels, but different microstructures, has not yet been reported.

Materials and methods

Processing of the EBM and wrought Ti–6Al–4V alloys

Rods of Ti–6Al–4V, 11 mm in diameter, were manufactured at the AM Center of Rotem Industries Ltd (Mishor Yamin, Israel) by EBM utilizing an Arcam Q20 Plus EBM machine and a

standard Grade 5 spherical powder with a size range of 45–106 μm. The rods were orientated in the XY plane of the tray. The EBM printing parameters are described in detail in Ref. [18]. Wrought Ti–6Al–4V Grade 23 (ASTM F136) rods, 11 mm in diameter, were produced by Dynamet Inc. The material certificate of the commercial alloy states that the alloy was annealed at 705 °C for 2 h and air cooled. Both EBM and wrought alloys contained ~6% β and similar impurity levels. The length of the α/β interphase boundaries in the EBM alloy was larger by 34% compared to that in the wrought alloy [22].

All samples were cut by electric discharge machining (EDM) to a thickness of 0.7 mm. After grinding to a thickness of 0.5 mm, diamond paste (down to 1 μm) was used to mechanically polish both sides. Prior to GC, the samples were rinsed in ethanol for 2 min in an ultrasonic bath.

Gaseous charging (hydrogenation)

GC was performed in a homemade Sievert apparatus consisting of a sealed autoclave and calibrated reservoir cell, as shown in Fig. 1 and described in Ref. [56]. High-purity gaseous hydrogen was used for the hydrogenation process. The examined samples were divided into two groups, one with only hydrogen dissolved in the alloy (i.e., without hydride formation), the other above the hydrogen solubility limit (i.e., with hydrides).

It was previously reported that hydride formation during GC of Ti–6Al–4V is in the range of 0.24–0.38 wt% (~10 to ~15 at%) hydrogen [28,57–60]. In Refs. [28,58,59], hydrogenation was conducted in the temperature range of 750–780 °C. Qazi et al. [28] reported that the β-phase content in the tested specimens was less than 7 vol%. Pushilina et al. [15] did not find any hydride phases following hydrogenation at 650 °C of EBM Ti–6Al–4V. The alloy contained 4 vol% β phase with 0.29 wt% hydrogen, indicating that hydrogen atoms primarily dissolved in the β_H phase. According to the pseudo-binary phase diagram of Ti–6Al–4V–xH proposed by Sun et al. [60], δ-hydride precipitates above ~0.3 wt% H at RT. Therefore, aiming to avoid hydride formation, the first group in this study was charged with lower hydrogen contents, namely 0.14 or 0.2 wt%. Hydrogenation to 0.32, 0.4, and 1.0 wt% H was carried out to form hydride phases. Hydrogenation was applied to a single specimen each time, in order to assure that it will absorb the desired hydrogen concentration. The hydrogenation procedure included two stages. First, the specimens were put into the autoclave and three purge cycles were performed using argon, prior to charging, to remove undesired gasses such as oxygen. The calibrated reservoir cell was filled by the desired quantity of hydrogen gas, in the range of ~4–30 [psi], that is required to obtain the desired concentration of each sample, based on sample's weight. This procedure was found to be accurate to control hydrogen concentration in previous studies [56]. The second stage involved heating the autoclave to 600 °C at a rate of ~20 °C/min and waiting another 15 min at 600 °C to achieve temperature homogeneity. Then, the specimen was exposed to the hydrogen gas by opening the isolation valve between the chambers. At this point, the autoclave was kept at 600 °C for another hour to achieve hydrogen homogeneity in the bulk. Following this step, the temperature was reduced to 500 °C for 15 min and then further reduced to 400 °C for another 15 min was performed. Finally, heating was stopped, and the autoclave was furnace cooled to RT. Low pressure values that were shown on the pressure gage indicated that the amount of the desired hydrogen was absorbed by the sample.

The time that elapsed between sample hydrogenation to full characterization was less than one month. It is expected that this time lag would not affect significantly the hydrogen content in the hydrogenated Ti–6Al–4V samples or its microstructure characteristics because: (1) no change in the X-ray diffraction (XRD) patterns of hydrogenated Ti–6Al–4V was observed after two months at RT [18,22]; (2) *in situ* XRD [61] and temperature programmed desorption (TPD) measurements [20] showed that hydrogen desorption is apparent only from ~200 °C.

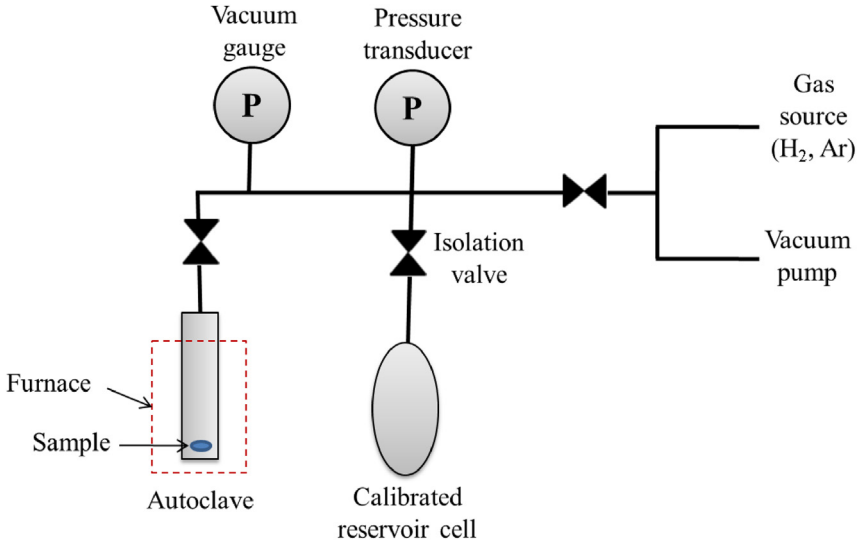

Fig. 1 – Schematic illustration of the Sievert apparatus for GC [56].

Material characterization

Detailed description of the microstructure, fractography and XRD characterization of EBM and wrought Ti–6Al–4V alloys is described in Ref. [22].

Chemical composition and density

Carbon, oxygen, nitrogen, and hydrogen content were measured by CS–800 carbon analyzer and ONH–2000 oxygen/nitrogen/hydrogen analyzer, respectively (Eltra GmbH, Haan, Germany), as described in Ref. [18]. The chemical composition of the major elements of the as-received alloys was confirmed by energy-dispersive X-ray spectroscopy (EDS). The density of the non-hydrogenated alloys was measured by the Archimedes method, using deionized (DI) water at RT.

Microstructural analysis by scanning electron microscopy (SEM) and XRD

The microstructure was characterized using SEM combined with EDS. Sample preparation for metallographic characterization included mechanical grinding and polishing down to 1 μm, followed by chemical etching in a solution of 2.5 N HNO_3 with 20 g/L NaF for 10–15 s. This solution is a mild version of the well-known Kroll's reagent, commonly used as an etchant to reveal the microstructure of Ti alloys [18].

XRD at RT was used for phase identification, phase content, and determination of lattice parameters. The XRD patterns of most samples were acquired by A D8 ADVANCE diffractometer with a Bragg-Brentano geometry (Bruker AXS, Madison, WI, USA) and Cu-Kα radiation source (λ = 1.5418 Å) was used. A linear position sensitive device (PSD) detector (LYNXEYE XE-T) was used, with an opening of 2.94°. Data points were acquired at increments of 0.02° and acquisition time of 0.25 s. The scan was within the range of 2θ = 20–90°. The XRD pattern of the EBM alloy that contained 1 wt% H was acquired by a powder diffractometer Empyrean (Panalytical B·V., Almelo, the Netherlands) equipped with X'Celerator position sensitive detector. Data points were collected in the θ/2θ geometry within the range of 2θ = 10–120°, using Cu- Kα radiation at 40 kV and 30 mA. The acquisition step was ~0.0167°, and the scan speed was 0.071°/s. The information is presented herein within the range of 33–65° to emphasize major changes.

The lattice parameters and phase content were fitted based on Rietveld refinement using TOPAS software, ver. 5 (Bruker AXS, Madison, WI, USA), fitting for the zero-error, lattice parameters, and phase composition. NIST Si 640e and LaB_6 660c standard reference materials were used to calibrate for peak position and peak shape, respectively. Peaks were fitted using a TCHZ function type, and the U,W,V and the asymmetry parameters were measured using LaB_6 660c and fixed to account for instrumental contributions to peak shape.

Mechanical behavior by SPT

The SPT technique is based on two (lower and upper) dies and a thin disk specimen (typically, 0.5 mm thick) that is locked in between them. During the test, a spherical cap punch is pushed into the specimen while the load and the punch stroke are monitored simultaneously until the end test criterion is achieved (e.g., maximal or failure load, a certain stroke, etc.). The small punch tests were performed on both non-hydrogenated and hydrogenated wrought and EBM Ti–6Al–4V samples at RT. The apparatus that was used is described in Refs. [49,62] in detail. A 2.4 mm in diameter hard steel ball was used. The geometry of the tested specimen, described in detail in Ref. [22], was a disk with a diameter of 11 mm and a thickness of 0.5 mm.

The SPT was conducted according to the following steps: (1) clamping of the specimen between the dies under 2500 N; (2) preload up to 30 N and balance the stroke transducer (Instron linear variable differential transducer, LVDT); and (3) pushing the ball into the specimen under stroke control at a speed of 0.1 mm/min up to failure. The relatively slow rate was selected in order to better capture any possible effects of hydrogen on the SPT curve in the early stages (zone I and II in the typical SPT curve described in Ref. [22]). Following specimen failure, the mode of fracture was characterized by SEM.

Results

Chemical composition and density

The content of light elements (C, H, O, and N) in the non-hydrogenated wrought and EBM Ti–6Al–4V alloys is given in Table 1. It can be seen that oxygen was the main impurity in both alloys, and that the total impurities content in both alloys was similar. The chemical composition of the major elements in the EBM alloy were (wt%) 90.1 Ti, 5.8 Al, and 4.1 V, in accordance with the ASTM F2924 specification [63]. The chemical composition of the major elements in the wrought alloy were (wt%) 90.0 Ti, 5.8 Al, and 4.2 V. The average densities of the EBM and wrought alloys were 4.421 ± 0.001 [22] and 4.423 ± 0.001 g/cm^3, respectively.

Microstructure

A SEM micrograph of the transverse cross-section of the wrought alloy before hydrogenation is shown in Fig. 2a. The microstructure consisted of two phases – α (darker, major) and β (brighter, minor). These phases were characterized by a higher Al content in the α phase and a higher vanadium content in the β phase (based on EDS analysis, also given in Ref. [22]). The β-phase morphology is discontinuous along the equiaxed α phase boundaries. A similar microstructure was reported before [64,65]. Fig. 2b–e reveal the microstructures of the wrought alloy hydrogenated to 0.2 wt% (Figs. 2b), 0.32 wt% (Fig. 2c and d), and 1 wt% (Fig. 2e and f) hydrogen. Since the microstructure of 0.14 wt% H was similar to that of 0.2 wt% H, it is not shown. An apparent increase of the bright area in Fig. 2b and a significant

Table 1 – Carbon and light elements composition (wt%) of the non-hydrogenated EBM and wrought Ti–6Al–4V alloys.

Element	Wrought	EBM [22]
C	0.0264 ± 0.0032	0.0063 ± 0.0002
O	0.1187 ± 0.0012	0.1092 ± 0.0175
H	0.0044 ± 0.0002	0.0036 ± 0.0004
N	0.0139 ± 0.0014	0.0322 ± 0.0025
Total	0.1634 ± 0.0060	0.1513 ± 0.0206

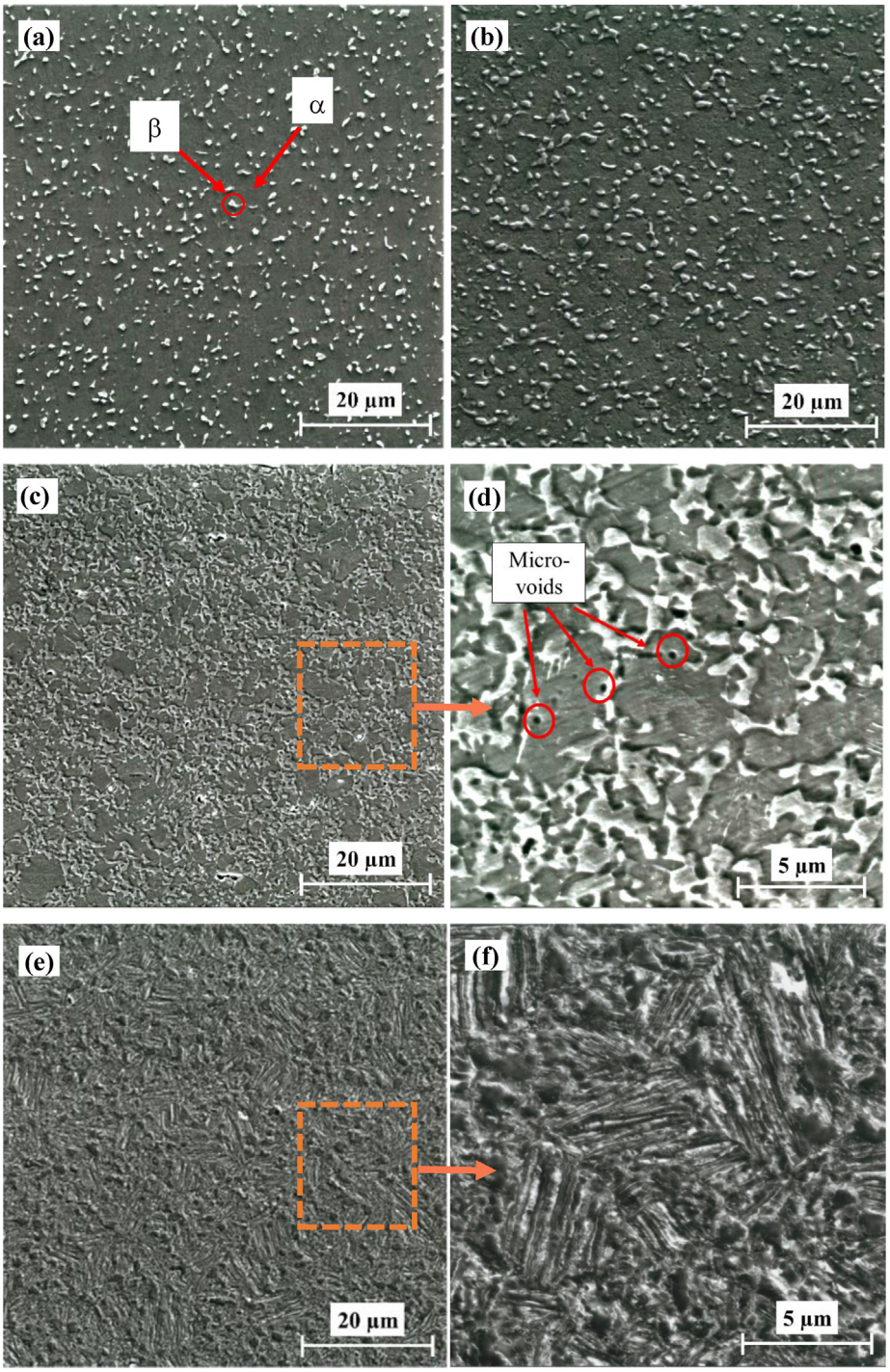

Fig. 2 – Cross-section SEM secondary electrons (SE) micrographs of wrought Ti–6Al–4V alloy. (a) Non-hydrogenated, (b) 0.20 wt% H, (c,d) 0.32 wt% H, (e,f) 1.00 wt% H.

increase of the bright area in Fig. 2c may indicate that β_H solid solution was formed, and its content increased, presumably as a result of the increase in the hydrogen content to 0.2 and 0.32 wt % hydrogen. This result is correlative with the XRD observations that will be discussed further in section Phase content and lattice parameters. The 0.2 wt% hydrogenated sample preserved the original morphology, whereas increasing the hydrogen content further to 0.32 wt% hydrogen increased significantly the brighter areas, indicating a higher β_H phase content (Fig. 2c and d). In addition to the increase of the β_H phase content, local microvoids were detected (highlighted in Fig. 2d, a higher magnification inset of Fig. 2c). Microvoids were also observed in electrochemically hydrogenated Ti–6Al–4V wrought and EBM alloys [18,22,40,42]. These microvoids are attributed to a volume shrinkage that occurs due to hydride precipitation from the a supersaturated β_H phase, as suggested by Brosh et al. [40]. Further increasing of the hydrogen content to 1.0 wt% changed the alloy microstructure, making it finer, as can

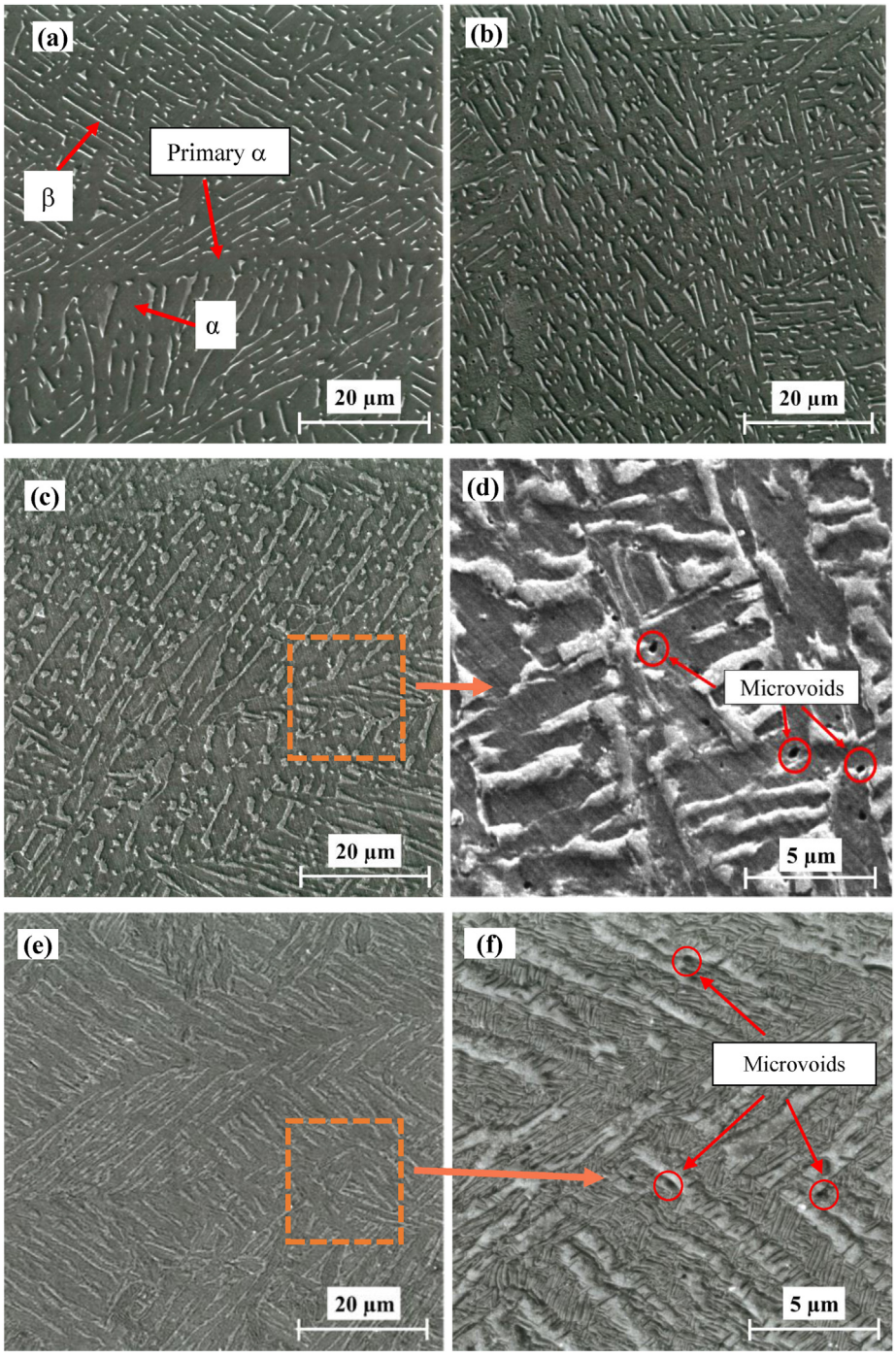

Fig. 3 – Cross-section SEM SE micrographs of EBM Ti–6Al–4V alloy. (a) Non-hydrogenated, (b) 0.20 wt% H, (c,d), 0.32 wt% H (e,f), 1.00 wt% H.

be seen in Fig. 2e, and at higher magnification in Fig. 2f. The homogeneous morphology with increasing hydrogen content is due to homogeneous hydrogen diffusion in the alloy due to the high-temperature GC. Niether cracks nor microstructural inhomogeneity were observed in the hydrogenated samples at all hydrogen contents.

SEM micrographs of the EBM alloy in the transverse orientation, before and after hydrogenation, are shown in Fig. 3. Fig. 3a reveals the microstructure of the non-hydrogenated EBM alloy. A lamellar α+β structure with a Widmanstätten morphology and primary α columnar, that was originated from prior β grains, oriented along the build direction, shown also in Ref. [22], is evident. The discontinuous morphology of the β-phase and the larger amount of α/β interphase boundaries in comparison to the wrought alloy are the outcome of rapid solidification in the EBM process. This morphology of EBM Ti–6Al–4V was also reported in Refs. [22,24,65,66]. Fig. 3b–f shows 0.2 wt% (Figs. 3b), 0.32 wt% (Fig. 3c and d), and 1 wt% (Fig. 3e and f) hydrogenated EBM alloys. An apparent enlargement of the bright area in Fig. 3b and a significant enlargement

of the bright area in Fig. 3c and d may indicate that a β_H phase (solid solution) was formed, and its content increased as a result of increasing the hydrogen content in the alloy. A similar effect was observed in the wrought alloy. The fundamental Widmanstätten structure at these hydrogen contents is preserved. These results are in agreement with the observations from XRD,which show that the β_H phase content increased from ~6 wt% in the non-hydrogenated alloy to ~13 wt% and ~18 wt% due to hydrogenation to 0.2 wt% and 0.32 wt% hydrogen content, respectively. After further increasing the hydrogen content to 1 wt%, the bright area appeared to be reduced and the microstructure became finer (see Fig. 3e and high-magnification Fig. 3f). The reduction in the β_H phase content at 1 wt% hydrogen agrees with the XRD observations (see section XRD phase analysis). The uniform morphology with increasing hydrogen content is due to uniform hydrogen diffusion in the alloy, as in the case of the wrought alloy. Neither cracks nor microstructural inhomogeneity were observed in the hydrogenated samples at any hydrogen content. Local microvoids were detected at 0.32 wt% H and above, similar to the wrought alloy (marked in Fig. 3d,f).

XRD phase analysis

Phase content and lattice parameters

Normalized XRD patterns (maximal peak is 100%) from the non-hydrogenated alloy and after GC of both wrought and EBM alloys are shown in Fig. 4. The ordinate values in this figure are after arbitrary scaling. Table 2 and Table 3 show the phase content and lattice parameters of the wrought and EBM alloys, respectively, calculated by TOPAS Rietveld refinement (with all R_{wp} values below 14.51). Both alloys showed a similar behavior as a function of hydrogen content up to 1.0 wt% H. The non-hydrogenated alloys contained two phases, α (major) and β (minor), similar to Ref. [22].

From Fig. 4 and Table 2 and 3, it can be seen that the lattice parameters of the hydrogenated hcp α-phase (ICDD 04-002-8708) were slightly larger with hydrogenation, both in the wrought and in the EBM alloys, as a result of α_H formation. It can be seen in Fig. 4 that all α_H peaks were broadened at 1.0 wt % hydrogen content. This can be attributed to elastic lattice strain [15,58] and/or an overlap of α_H and α_2 reflections. Fig. 5a (data is taken from Tables 2 and 3) presents the α/α_H phase quantity as a function of hydrogen content in both alloys. It is evident from Fig. 5a that the α_H-phase quantity in the wrought alloy was gradually reduced from 94.7 wt% in the non-hydrogenated alloy to 41.2 wt% in the 1 wt% hydrogenated alloy, and from 94.3 wt% to 37.4 wt% in the EBM alloy. Thus, the total content of the α/α_H phase was reduced by 56–60% due to hydrogenation to 1 wt%.

From Fig. 4 and Tables 2 and 3, the lattice parameter a of the hydrogenated bcc β-phase (ICDD 00-044-1288) increased with hydrogenation by 4% in both alloys, indicating the formation of β_H solid solution. The phase shifts toward smaller angles due to the solution of hydrogen atoms was also observed by Pushilina et al. [15] and Sun et al. [60]. Fig. 5b (data is taken from Tables 2 and 3) presents the β/β_H phase quantity as a function of hydrogen content in both alloys. It is seen from Fig. 5b that the β_H phase quantity was gradually increased up to 0.4 wt% hydrogen content, from 5.3 wt% and 5.7 wt% to 18.0 wt% and 22.6 wt% in the hydrogenated wrought and EBM alloys, respectively. Further hydrogenation to 1 wt% hydrogen content was followed by reducing the β_H quantity to 8.2 wt% and 14.8 wt% in the wrought and EBM alloys, respectively. Thus, the total content of the β/β_H phase was increased to a maximum by 3.4–4 times at 0.4 wt% hydrogen content, and then reduced.

The reflection at $2\theta = 36.5^\circ$ at 0.32, 0.4, and 1 wt% hydrogen contents, shown in Fig. 4, is attributed to the tetragonal γ hydride (ICDD 00-040-1244), in agreement with Pushilina et al. [15] and Metalnikov et al. [20].

The reflections at $2\theta = 35.5^\circ$ and $2\theta = 60.0^\circ$ at 1 wt% hydrogen content are attributed to the fcc δ hydride (ICDD 01-071-4960), formed from the α or β phase, depending on the hydrogen content [14].

At 1 wt% hydrogen content, an additional peak at $2\theta = 25.8^\circ$ (not shown here) was observed. This peak is attributed to a reflection from the (011) plain of the α_2 phase (ICDD 04-004-2732) associated with Al enrichment of the primary α phase [15].

Hydrogen saturation in the β_H phase

Fig. 6 shows the β/β_H lattice parameter of both the wrought and EBM Ti–6Al–4V alloys as a function of hydrogen content. It is evident that the lattice parameters in both alloys increased linearly up to hydrogen content of 0.2 wt%. Further increasing of the hydrogen content to 0.32 wt% resulted in an increase of the lattice parameter, albeit deviating from the linear trend that is seen up to 0.2 wt% hydrogen content. Further increase of the hydrogen content up to 1 wt% did not affect the lattice parameter significantly. This suggests that the β_H solid solution reached hydrogen saturation at hydrogen content between 0.2 and 0.32 wt%. The average lattice parameter of the saturated β_H phase (i.e., at 0.32 wt% hydrogen content) was 3.315 Å (calculated from both alloys). Fig. 6b shows the linear growth and curve-fitting of the average β/β_H lattice parameters in both alloys, up to 0.2 wt% H, with a Pearson's value $r = 0.995$. This linear correlation was also observed by Zhu and Li [58] for the forged Ti–6Al–4V alloy. The intercept between the value of the lattice parameter of the saturated β_H phase (3.315 Å) with the linear curve growth of the β_H lattice parameter below 0.32 wt% H (namely, at 0.27 wt% H) represents the hydrogen saturation value of the β_H phase. This value is within the range reported in the literature (0.24–0.38 wt% [28,57–60]). Therefore, hydride formation is expected above 0.27 wt% H.

SPT curves

The SPT (load-displacement) curves of non-hydrogenated and GC wrought and EBM alloys are shown in Fig. 7a and b, respectively. The curves of the non-hydrogenated alloys are similar to those reported in Refs. [22,54]. It is evident from Fig. 7 that the mechanical behavior of both alloys can be divided into two groups: the first is for the non-hydrogenated and the hydrogenated alloys up to 0.2 wt% hydrogen content, and the second is for the hydrogenated alloys from 0.32 wt% up to 1 wt%. The SPT curves in the first group are similar, exhibiting a ductile material behavior. Further increasing of the hydrogen content up to 1 wt% led to a substantial

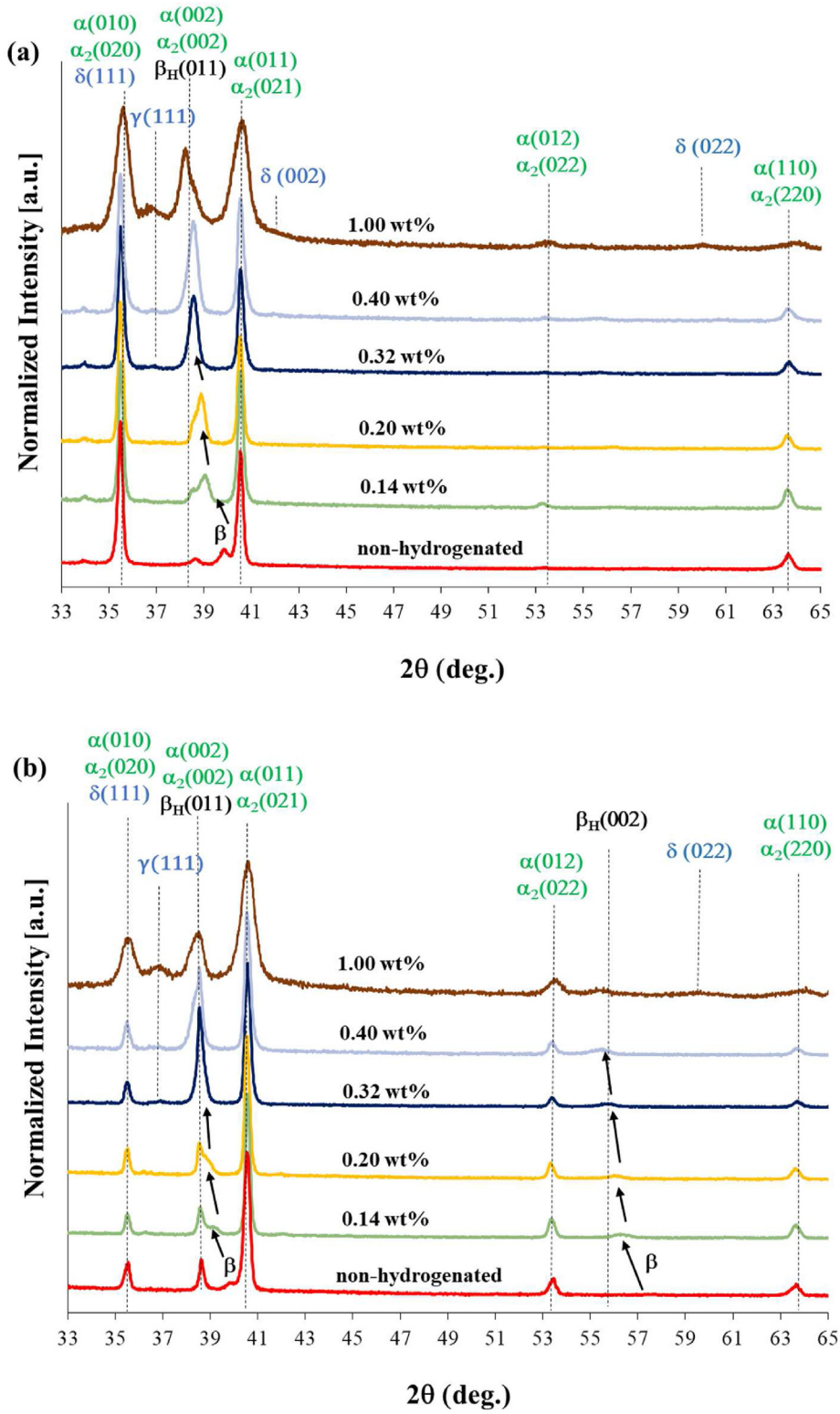

Fig. 4 – XRD patterns of non-hydrogenated and hydrogenated wrought (a) and EBM (b) Ti–6Al–4V alloys as a function of hydrogen content.

degradation in the mechanical properties, including maximum load (P_{max}), displacement at maximum load (δ_{max}) and absorbed energy (E).

The effect of hydrogen content on the mechanical properties of both alloys is shown in Fig. 8. Fig. 8a shows changes in P_{max}, while Fig. 8b shows δ_{max}, and Fig. 8c shows E (the area under the load-displacement curve up to the maximum load). Both alloys exhibited similar trends in all three properties, with higher values up to hydrogen content of 0.2 wt%. The mechanical properties degraded following a further increase

Table 2 – Lattice parameters and phase content of the non-hydrogenated and hydrogenated *wrought* alloys.

Wrought	$\alpha/\alpha_H/\alpha_2$	β/β_H	Ti-hydrides
Non-hydrogenated	94.67 wt% $a = 2.925$ Å $c = 4.670$ Å	5.33 wt% $a = 3.189$ Å	–
0.14 wt%	94.69 wt% $a = 2.927$ Å $c = 4.688$ Å	5.31 wt% $a = 3.257$ Å	–
0.20 wt%	89.89 wt% $a = 2.929$ Å $c = 4.683$ Å	10.11 wt% $a = 3.286$ Å	–
0.32 wt%	83.39 wt% $a = 2.927$ Å $c = 4.678$ Å	16.61 wt% $a = 3.317$ Å	$\gamma < 2.00$ wt%
0.40 wt%	81.97 wt% $a = 2.927$ Å $c = 4.675$ Å	18.03 wt% $a = 3.312$ Å	$\gamma < 2.00$ wt%
1.00 wt%	α: 41.17 wt% $a = 2.923$ Å $c = 4.698$ Å $\alpha 2$: 29.98 wt% $a = 5.806$ Å $c = 4.645$ Å	8.22 wt% $a = 3.313$ Å	γ: 3.01 wt% a = 3.980 c = 4.867 δ: 17.62 wt% $a = 4.355$ Å

Table 3 – Lattice parameters and phase content of the non-hydrogenated and hydrogenated *EBM* alloys.

EBM	$\alpha/\alpha_H/\alpha 2$	β/β_H	Ti -hydrides
Non-hydrogenated	94.26 wt% $a = 2.927$ Å $c = 4.669$ Å	5.74 wt% $a = 3.199$ Å	–
0.14 wt%	92.24 wt% $a = 2.926$ Å $c = 4.679$ Å	7.76 wt% $a = 3.247$ Å	–
0.20 wt%	87.42 wt% $a = 2.928$ Å $c = 4.681$ Å	12.58 wt% $a = 3.283$ Å	–
0.32 wt%	81.68 wt% $a = 2.926$ Å $c = 4.681$ Å	18.32 wt% $a = 3.308$ Å	$\gamma < 2.00$ wt%
0.40 wt%	77.44 wt% $a = 2.925$ Å $c = 4.678$ Å	22.56 wt% $a = 3.316$ Å	$\gamma < 2.00$ wt%
1.00 wt%	α: 37.39 wt% $a = 2.935$ Å $c = 4.672$ Å $\alpha 2$: 32.11 wt% $a = 5.820$ Å $c = 4.673$ Å	14.81 wt% $a = 3.327$ Å	γ: 2.58 wt% a = 4.062 c = 4.900 δ: 13.00 wt% $a = 4.372$ Å

in the hydrogen content up to 1 wt%. Following hydrogenation to 0.32 wt% hydrogen, the maximum load of the wrought alloy decreased by 49% (from 1.43 to 0.73 kN) and the displacement at maximum load decreased by 28% (from 0.76 to 0.55 mm); *E* decreased by more than 50% (from 1.30 to 0.55 J/mm). For the EBM alloy, the maximum load decreased by 33% (from 1.17 to 0.78 kN), the displacement at maximum load decreased by 46% (from 0.99 to 0.53 mm), and *E* decreased by more than 50% (from 1.64 to 0.75 J/mm). Following hydrogenation to 1.0 wt% hydrogen content of both alloys, *E* decreased by more than 96% (from 1.30 to 0.05 J/mm in the wrought alloy, and from 1.64 to 0.03 J/mm in the EBM alloy).

It should be noted that the degradation in the mechanical behavior of hydrogenated alloys was significant above 0.32 wt % hydrogen content. This behavior supports the β_H hydrogen saturation point at 0.27 wt% discussed above, thus the degradation in mechanical properties is due to hydride formation beyond the solubility limit. The SPT results emphasize the advantages of this technique due its sensitivity to the small hydride content (γ hydride is < 2.0 wt% at 0.32 wt% hydrogen content). Considering the findings above, it can be concluded that both the wrought and EBM alloys exhibit similar mechanical behavior, with degradation above the β_H hydrogen saturation point at 0.27 wt%.

Fractography

Fig. 9 shows the fracture morphology and fracture surfaces (fractography) of both hydrogenated and non-hydrogenated wrought alloy following SPT. The non-hydrogenated wrought alloy shows a typical ductile fracture (Fig. 9a–c) similar to that reported for the non-hydrogenated wrought alloy in Ref. [22]. The top-view morphology of the fracture is semi-circular (Fig. 9a), and at high magnification the fracture is characterized by dimples, as seen in Fig. 9c. The fracture morphology of the 0.2 wt% H alloy (Fig. 9d–f) is similar to that of the non-hydrogenated alloy, i.e. it is characteristic of ductile materials. These findings are in agreement with the XRD and P_{max}, δ_{max} and *E* values reported above, for the ductile wrought alloys below 0.32 wt% hydrogen content.

The top view fracture morphology and fracture surfaces of the 0.32 wt% and 1.0 wt% H alloys are shown in Fig. 9g–i and Fig. 9j-l, respectively. These figures show a fundamental change in the fracture mode. Top-view fracture morphology (Fig. 9g) is characterized by a *star-like* shape, and at high magnification the fracture surfaces are typical of a quasi-cleavage failure (Fig. 9i), which is attributed to hydride presence. For the 1.0 wt% content alloy, no dimples were evident (Fig. 9l), indicating more severe embrittlement due to a higher hydrides content. The fracture morphologies observed above 0.32 wt% H are typical of brittle materials [22,47,48]. These findings are in agreement with the XRD data and P_{max}, δ_{max} and *E* values reported above for the brittle wrought alloys obtained above 0.2 wt% hydrogen content. The brittle fracture morphology of the GC alloys is different from the brittle fracture characteristics reported in Ref. [22] for the EC alloy due to the absence of a hydride layer on the surface in the present study, which was typical of EC Ti–6Al–4V.

The fractography (SEM) of the EBM alloy after SPT is shown in Fig. 10. The top-view of the fracture and mode of fracture of the non-hydrogenated (Fig. 10a–c) and the 0.2 wt% H alloys (Fig. 10d–f) were similar, showing a ductile behavior. The top-view of the fracture in alloys hydrogenated up to 0.2 wt% H (Fig. 10a,d) showed semi-circular and radial cracks. At high magnification, the fracture was characterized by a mix-mode fracture (ductile and brittle fracture), similar to that reported

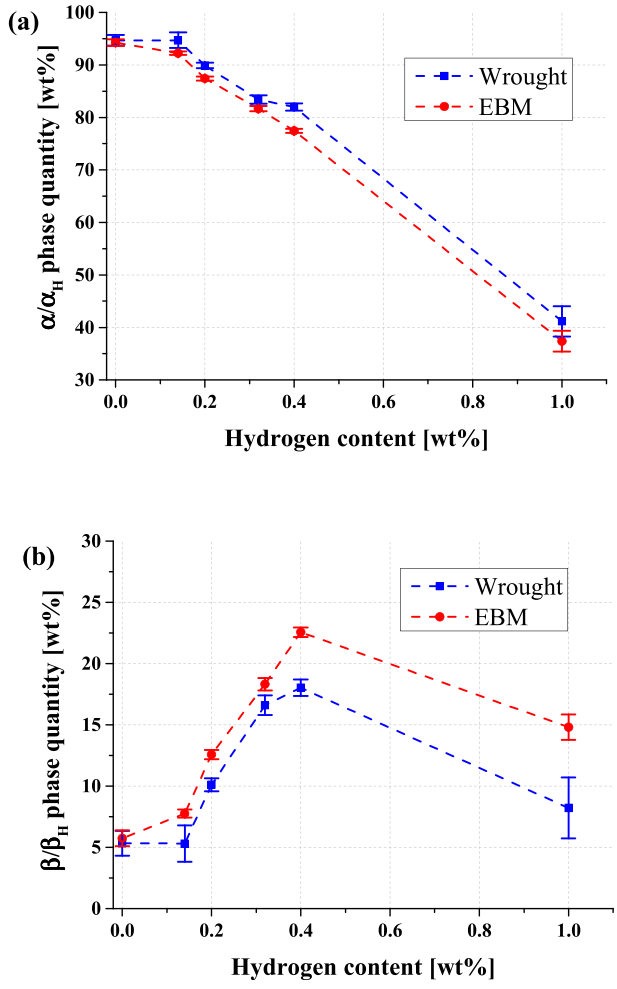

Fig. 5 – Phase content as a function of hydrogen content. (a) α/α_H, (b) β/β_H.

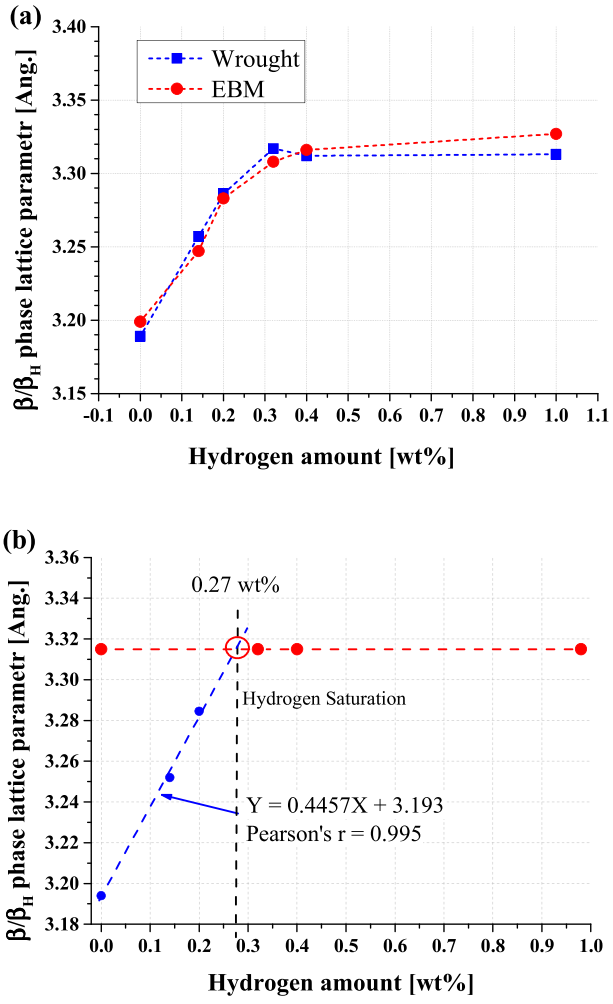

Fig. 6 – (a) β/β_H phase lattice parameter in the wrought and EBM Ti–6Al–4V alloys as a function of hydrogen content. (b) The linear growth region of the lattice parameters of the β/β_H and saturated β_H phases.

for the non-hydrogenated EBM alloy in Ref. [22]. The top-view fracture in the EBM alloy hydrogenated up to 0.2 wt% H (Fig. 10a,d) was different from that in the wrought alloy (Fig. 9a,d) due to differences in their original microstructure, as discussed in detail in Ref. [22]. These findings are also in agreement with the XRD, P_{max}, δ_{max} and E results discussed above for the ductile EBM alloys hydrogenated below 0.32 wt% H. Increasing the hydrogen content to 0.32 wt% and above changed the fracture morphology from ductile to brittle (Fig. 10g–i). The top-view fracture of 0.32 wt% content alloy (Fig. 10g) changed from semi-circular and radial cracks to star-like morphology. The fracture exhibited a mix mode, combining dimples and cleavage structure. Further increasing the hydrogen content to 1.0 wt% (Fig. 10j-l) increased the brittle morphology, similar to the wrought alloy. The top-view fracture became pure star-like, and dimples were not identified at high magnification (Fig. 10l). These findings are also in agreement with the XRD, P_{max}, δ_{max} and E results reported above for the brittle EBM alloys hydrogenated to more than 0.2 wt% H.

Discussion

The influence of gaseous hydrogen charging at 600 °C on the microstructure and mechanical behavior of wrought and EBM Ti–6Al–4V alloys was investigated at 0.14, 0.20, 0.32, 0.4, and 1.0 wt% hydrogen content. Both alloys contained ~6 wt% β phase and similar impurity levels in their non-hydrogenated counterpart, allowing the exclusion of compositional effects on the alloys' susceptibility to hydrogenation. On the other hand, the EBM alloy contained 34% more α/β interphase boundaries than the wrought alloy.

Both alloys showed similar phase content and trends in mechanical behavior at all hydrogen contents. After hydrogenation, α_H and β_H solid solutions were formed. The α_H phase (major phase) quantity reduced gradually with hydrogen content while increasing the β_H content and/or forming α_2 and hydrides due to the low solubility of hydrogen in the major α

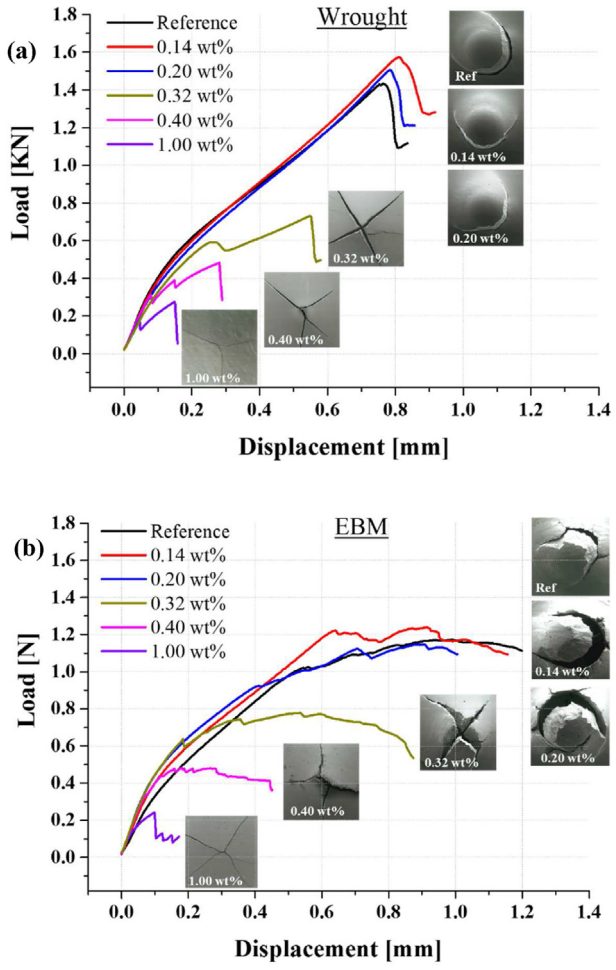

Fig. 7 – SPT curves of non-hydrogenated and hydrogenated wrought (a) and EBM (b) Ti– 6Al–4 alloys. SEM insets: top-view fracture morphologies.

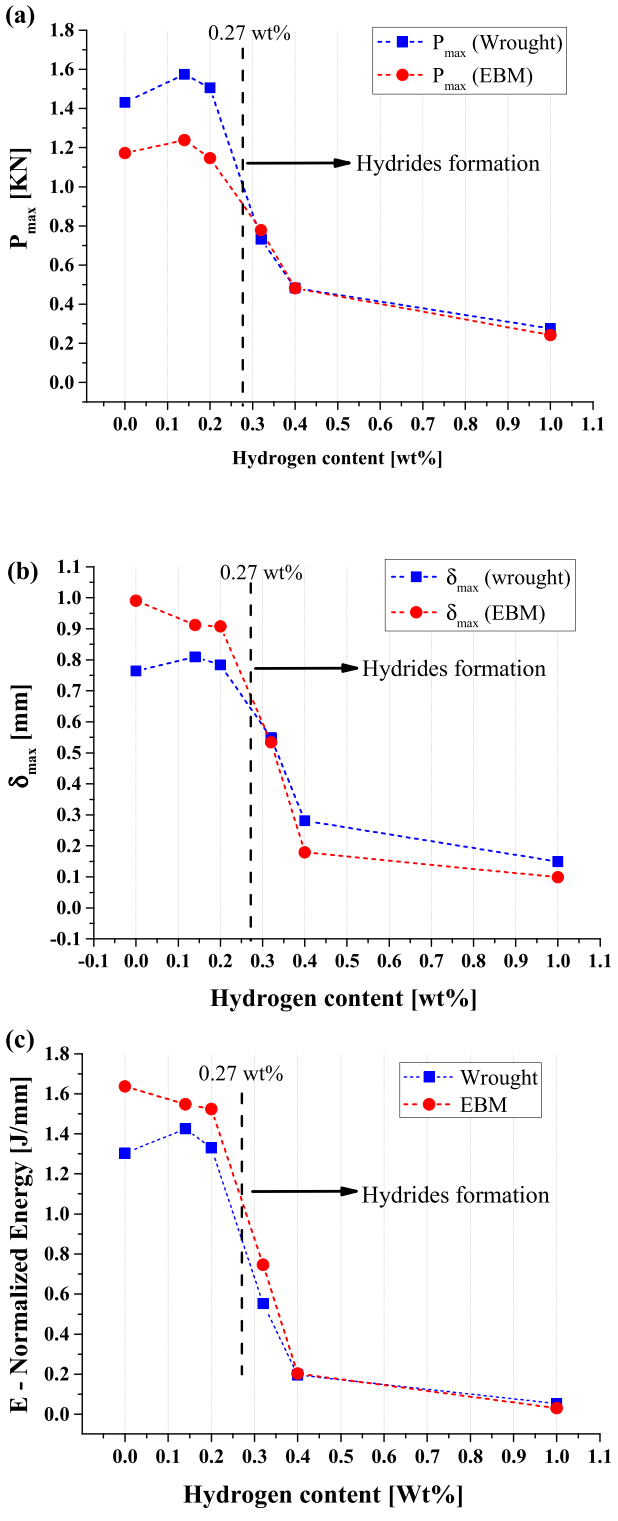

Fig. 8 – The effect of hydrogen content on the mechanical behavior of wrought and EBM Ti–6Al–4 alloys. (a) Maximum load, (b) displacement at maximum load, and (c) normalized absorbed energy.

phase. The transformation of the α and β phases during gaseous charging and its dependence on hydrogen content has been explained elsewhere in detail [13,15,67]. At the same time, the β_H phase content increased up to 0.4 wt% H due to the tendency of hydrogen to stabilize the β_H solid solution in Ti–6Al–4V, in agreement with [67]. Further increasing of the hydrogen content from 0.4 to 1.0 wt% led to decrease in the amount of the β_H, in agreement with [15]. The reduction in the β_H content at higher hydrogen content was attributed to hydride formation (e.g., γ hydride, minor) at 0.32 wt% hydrogen content and above. The δ hydride and α_2 phases formed at 1.0 wt% H.

Microstructure observations revealed that hydrogenation led to microvoid formation in both alloys at 0.32 wt% and above. This can be attributed to a local shrinkage due to hydride precipitation from the hydrogen-supersaturated β_H phase, as suggested by Brosh et al. [40]. The β_H solid solution was saturated at 0.27 wt% H, below which no hydrides or other phases exist except for α_H. This matches the β_H saturation range reported in the literature, 0.24–0.38 wt% [28,57–60].

The P_{max}, δ_{max} and E values for both the wrought and EBM alloys hydrogenated up to 0.2 wt% H (i.e, below the β_H solubility limit where hydrides form) were characterized by relatively high strength and ductility, similar to the non-hydrogenated counterparts' alloys. The similarity in values within the range of 0–0.2 wt% H are due to the absence of hydrides. This agrees with a previous report [68] of the absence of degradation in

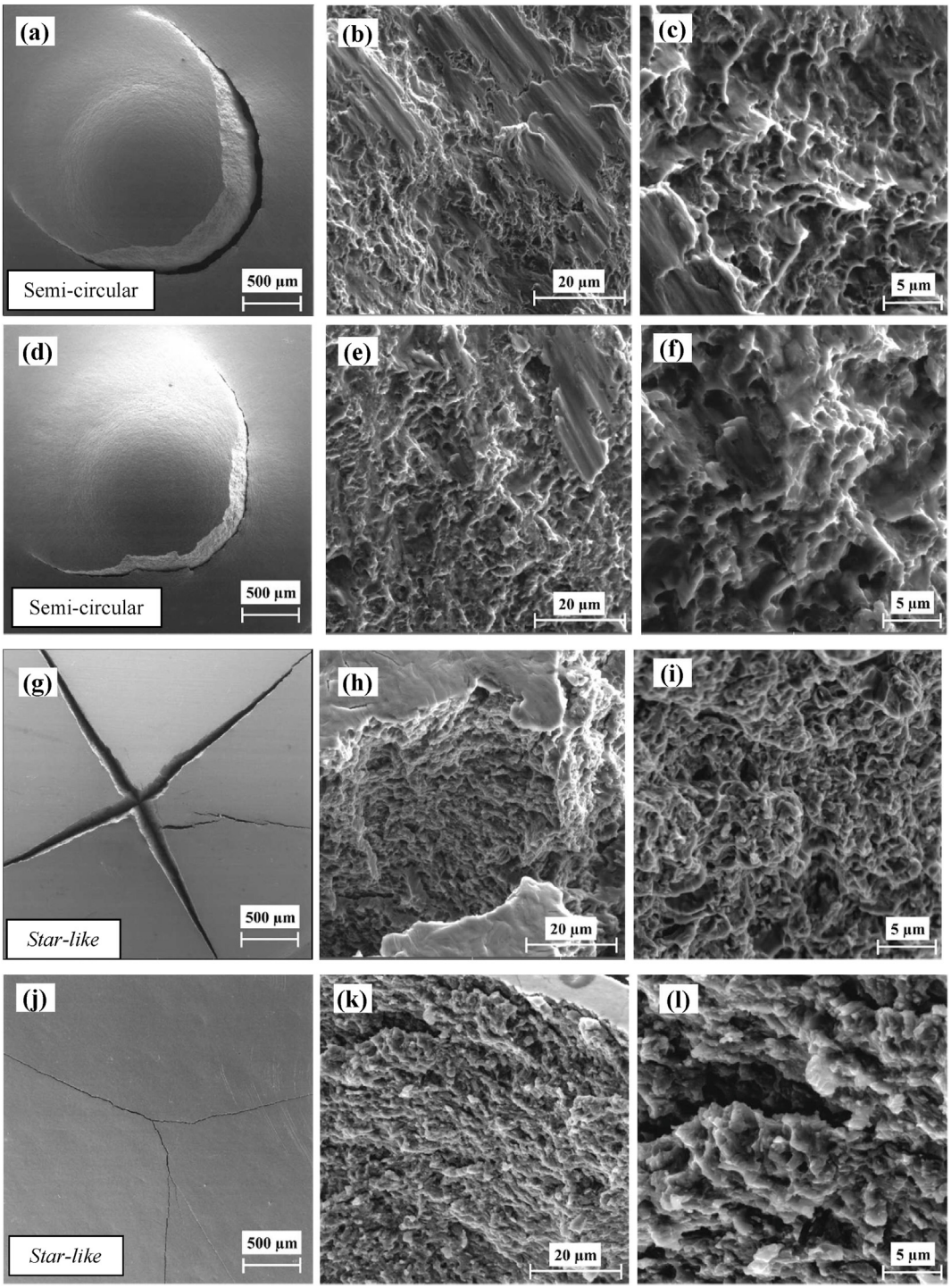

Fig. 9 – SEM fractography of wrought Ti–6Al–4V alloy after SPT. (a–c) Non-hydrogenated, (d–f) 0.20 wt% H, (g–i) 0.32 wt% H, (j–l) 1.0 wt% H.

tensile properties of Ti–6Al–4V hydrogenated from the gas phase at 600 °C up to 0.2 wt% H. Above the β_H hydrogen solubility limit, the mechanical parameters P_{max}, δ_{max}, and E degraded significantly due to hydride formation in both alloys. This is in agreement with the report in Ref. [67] on the degradation of mechanical properties of Ti–6Al–4V hydrogenated from the gas phase performed at 750 °C to 0.3 wt% and above, where hydride formation occurred.

Our current study emphasizes the different effects of gaseous (high temperatures) and electrochemical (RT) hydrogenation on the susceptibility of Ti–6Al–4V alloys that contain similar composition and phase content to HE. In our previous work, we studied the effect of EC at RT on the same wrought and EBM alloys [22]. It was found that the EBM alloy is more susceptible to HE than the wrought alloy. It was shown that the formation of a layer with high

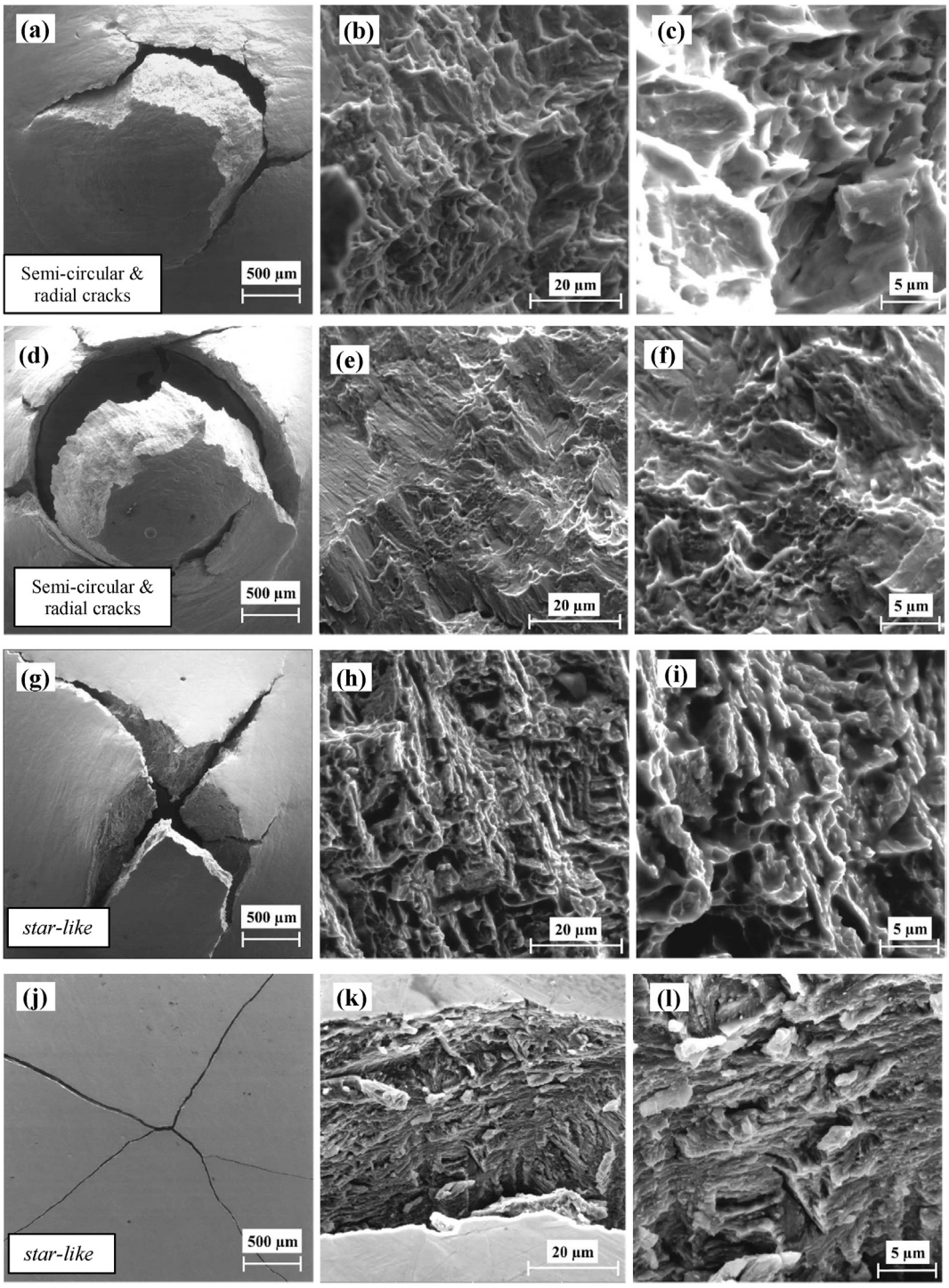

Fig. 10 – SEM fractography of EBM Ti–6Al–4V alloy after SPT. (a–c) Non-hydrogenated, (d–f) 0.20 wt% H, (g–i) 0.32 wt% H, (j–l) 1.0 wt% H.

concentrations of δ_a and δ_b hydrides on the wrought alloy surface acted as a barrier to hydrogen diffusion into the bulk of the alloy, thus inhibiting further hydrogen damage compared to the EBM alloy. The surface layer on the wrought alloy was formed due to the combination of the lower amount of α/β interphase boundaries compared to that in the EBM alloy, and thus slower hydrogen diffusion at RT. In the current study, GC at high temperature was used, and the diffusion coefficients were significantly higher than those at RT. Thus, the microstructural differences did not have significant effects on hydrogen diffusion into the bulk, resulting in similar mechanical behavior. Therefore, the wrought alloy loses its structural advantages over the EBM alloy w.r.t. HE when high-temperature GC is involved.

Conclusions

The influence of gaseous hydrogenation on the microstructure and mechanical behavior of EBM AM'ed and wrought Ti–6Al–4V alloys containing ~6 wt% β and similar impurity levels, but 34% higher amount of α/β interphase boundaries length in the EBM alloy, was studied. The main conclusions are listed below.

1. Both EBM and wrought Ti–6Al–4V alloys showed a similar phase content and mechanical behavior at all hydrogen contents, despite the original microstructural differences.
2. β_H became saturated at 0.27 wt% hydrogen content.
3. Both alloys exhibited high strength and ductility up to hydrogen content of 0.2 wt%, prior to β_H saturation concentration. Above the β_H saturation concentration, the mechanical properties P_{max}, δ_{max} and E degraded significantly due to hydrides formation.
4. Both wrought and EBM Ti–6Al–4V alloys had similar mechanical behavior when gaseous hydrogen charging was involved, in contrast to electrochemical hydrogen charging where the wrought alloy showed higher resistivity to HE.
5. The influence of hydrogen on the mechanical behavior of wrought and EBM Ti–6Al–4V alloys is highly dependent on the hydrogen charging method: electrochemical at RT or gaseous at high temperature. This is due to uniform hydrogen uptake in the bulk alloy at high temperatures, while in EC, hydride layers developed on the outer surface and acted as barrier layers that hindered hydrogen absorption. Therefore, the wrought alloy lost its advantage over the EBM alloy with respect to HE when high-temperature gaseous charging is used.

Declaration of competing interest

The authors declare that they have no known competing financial interests or personal relationships that could have appeared to influence the work reported in this paper.

Acknowledgements

This work was supported by grant No. 322/20 from the Pazy Foundation of the Israel Atomic Energy Commission and the Israeli Council of Higher Education. We thank Mr. David Hai David and Mr. Maymon Cohen for their technical assistance, Dr. Eitan Tiferet, Mr. Michael Chonin and Mr. Yaron I. Ganor for EBM of Ti–6Al–4V, Dr. Yelena Mirsky and Dr. Lonia Friedlander for XRD measurements, Mr. Nadav Guy for gas analysis, and Mr. David Noiman for density measurments.

REFERENCES

[1] Boyer RR. An overview on the use of titanium in the aerospace industry. Mater Sci Eng, A 1996;213(1):103–14.
[2] Eliaz N. Corrosion of metallic biomaterials: a review. Materials 2019;12(3):407.
[3] Hong SB, Eliaz N, Sachs EM, Allen SM, Latanision RM. Corrosion behavior of advanced titanium-based alloys made by three-dimensional printing (3DP™) for biomedical applications. Corrosion Sci 2001;9(43):1781–91.
[4] Donachie MJ. Titanium: a technical guide. 2nd ed. ASM International; 2000.
[5] Rack HJ, Qazi JI. Titanium alloys for biomedical applications. Mater Sci Eng C 2006;26(8):1269–77.
[6] Lütjering G. Influence of processing on microstructure and mechanical properties of (α+β) titanium alloys. Mater Sci Eng, A 1998;243(1):32–45.
[7] Luan JH, Jiao ZB, Liu WH, Lu ZP, Zhao WX, Liu CT. Compositional and microstructural optimization and mechanical-property enhancement of cast Ti alloys based on Ti-6Al-4V alloy. Mater Sci Eng, A 2017;704:91–101.
[8] Chong Y, Bhattacharjee T, Shibata A, Tsuji N. Investigation of the grain size effect on mechanical properties of Ti-6Al-4V alloy with equiaxed and bimodal microstructures. IOP Conf Ser Mater Sci Eng 2017;219(1):012013.
[9] Paramore JD, Fang ZZ, Sun P, Koopman M, Chandran KSR, Dunstan M. A powder metallurgy method for manufacturing Ti-6Al-4V with wrought-like microstructures and mechanical properties via hydrogen sintering and phase transformation (HSPT). Scripta Mater 2015;107:103–6.
[10] Assis SL de, Wolynec S, Costa I. Corrosion characterization of titanium alloys by electrochemical techniques. Electrochim Acta 2006;51(8):1815–9.
[11] Tal-Gutelmacher E, Eliezer D. The hydrogen embrittlement of titanium-based alloys. JOM 2005 Sep 1;57(9):46–9.
[12] Madina V, Azkarate I. Compatibility of materials with hydrogen. Particular case: hydrogen embrittlement of titanium alloys. Int J Hydrogen Energy 2009;34(14):5976–80.
[13] Luo L, Su Y, Guo J, Fu H. Formation of titanium hydride in Ti–6Al–4V alloy. J Alloys Compd 2006;425(1–2):140–4.
[14] Liu HJ, Zhou L, Liu P, Liu QW. Microstructural evolution and hydride precipitation mechanism in hydrogenated Ti–6Al–4V alloy. Int J Hydrogen Energy 2009;34(23):9596–602.
[15] Pushilina N, Panin A, Syrtanov M, Kashkarov E, Kudiiarov V, Perevalova O, Laptev R, Lider A, Koptyug A. Hydrogen-induced phase transformation and microstructure evolution for Ti-6Al-4V parts produced by electron beam melting. Metals 2018;8(5):301.
[16] Okamoto H. H-Ti (hydrogen-titanium). J Phase Equilibria Diffus 2011;32(2):174.
[17] Silverstein R, Eliezer D. Hydrogen trapping in 3D-printed (additive manufactured) Ti-6Al-4V. Mater Char 2018;144:297–304.
[18] Navi NU, Tenenbaum J, Sabatani E, Kimmel G, Ben David R, Rosen BA, Barkay Z, Ezersky V, Tiferet E, Ganor YI, Eliaz N. Hydrogen effects on electrochemically charged additive manufactured by electron beam melting (EBM) and wrought Ti–6Al–4V alloys. Int J Hydrogen Energy 2020;45(46):25523–40.
[19] Metalnikov P, Eliezer D, Ben-Hamu G, Tal-Gutelmacher E, Gelbstein Y, Munteanu C. Hydrogen embrittlement of electron beam melted Ti–6Al–4V. J Mater Res Technol 2020;9(6):16126–34.
[20] Metalnikov P, Eliezer D, Ben-Hamu G. Hydrogen trapping in additive manufactured Ti–6Al–4V alloy. Mater Sci Eng, A 2021;811:141050.
[21] Laptev R, Kudiiarov V, Pushilina N. Hydrogen influence on defect structure and mechanical properties of EBM Ti-6Al-4V. Mater Today Proc 2019;19:2084–8.
[22] Lulu-Bitton N, Sabatani E, Rosen BA, Kostirya N, Agronov G, Tiferet E, Eliaz N, Navi NU. Mechanical behavior of

electrochemically hydrogenated electron beam melting (EBM) and wrought Ti–6Al–4V using small punch test. Int J Hydrogen Energy 2022;47(9):6388–403.
[23] Fukai Y. Metal-hydrogen system under extended p, T conditions. In: The metal-hydrogen system: basic bulk properties. Berlin, Heidelberg: Springer; 2005. p. 91–145.
[24] Pushilina N, Syrtanov M, Kashkarov E, Murashkina T, Kudiiarov V, Laptev R, Lider A, Koptyug A. Influence of manufacturing parameters on microstructure and hydrogen sorption behavior of electron beam melted titanium Ti-6Al-4V alloy. Materials 2018;11(5):763.
[25] Kim J, Tasan CC. Microstructural and micro-mechanical characterization during hydrogen charging: an in situ scanning electron microscopy study. Int J Hydrogen Energy 2019;44(12):6333–43.
[26] Kim J, Plancher E, Tasan CC. Hydrogenation-induced lattice expansion and its effects on hydrogen diffusion and damage in Ti–6Al–4V. Acta Mater 2020;188:686–96.
[27] Kim J, Kang J, Tasan CC. Hydride formation in Ti6Al4V: an in situ synchrotron X-ray diffraction study. Scripta Mater 2021;193:12–6.
[28] Qazi JI, Rahim JSAM, Fores FH, Senkov ON, Genc A. Phase transformations in Ti-6Al-4V-xH alloys. Metall Mater Trans A 2001;32(10):2453–63.
[29] Eliaz N, Foucks N, Geva D, Oren S, Shriki N, Vaknin D, Fishman D, Levi O. Comparative quality control of titanium alloy Ti-6Al-4V, 17-4 PH stainless steel, and aluminum alloy 4047 either manufactured or repaired by laser engineered net shaping (LENS). Materials 2020;13(18):4171.
[30] Bandyopadhyay A, Traxel KD, Lang M, Juhasz M, Eliaz N, Bose S. Alloy design via additive manufacturing: advantages, challenges, applications and perspectives. Mater Today 2022;52:207–24.
[31] Svetlizky D, Das M, Zheng B, Vyatskikh AL, Bose S, Bandyopadhyay A, Schoenung JM, Lavernia EJ, Eliaz N. Directed energy deposition (DED) additive manufacturing: physical characteristics, defects, challenges and applications. Mater Today 2021;49:271–95.
[32] Svetlizky D, Zheng B, Vyatskikh A, Das M, Bose S, Bandyopadhyay A, Schoenung JM, Lavernia EJ, Eliaz N. Laser-based directed energy deposition (DED-LB) of advanced materials. Mater Sci Eng, A 2022;840:142967.
[33] Lewandowski JJ, Seifi M. Metal additive manufacturing: a review of mechanical properties. Annu Rev Mater Res 2016;46:151–86.
[34] Tevet O, Svetlizky D, Harel D, Barkay Z, Geva D, Eliaz N. Measurement of the anisotropic dynamic elastic constants of additive manufactured and wrought Ti6Al4V alloys. Materials 2022;15(2):638.
[35] Pushilina NS, Stepanova EN, Kudiiarov VN, Laptev RS, Syrtanov MS. Heat treatment of the Ti-6Al-4V alloy manufactured by electron beam melting. In: AIP conf proceed 2167. AIP Publishing LLC; 2019, 020290.
[36] Bilgin GM, Esen Z, Akın ŞK, Dericioglu AF. Optimization of the mechanical properties of Ti-6Al-4V alloy fabricated by selective laser melting using thermohydrogen processes. Mater Sci Eng, A 2017;700:574–82.
[37] Gaddam R, Åkerfeldt P, Pederson R, Antti ML. Influence of hydrogen environment on the mechanical properties of cast and electron beam melted Ti-6Al-4V. In: World conf on titanium: 19/06/2011-24/06/2011. Social Sciences Academic Press (China); 2012. p. 1885–8.
[38] Navi NU, Rosen BA, Sabatani E, Tenenbaum J, Tiferet E, Eliaz N. Thermal decomposition of titanium hydrides in electrochemically hydrogenated electron beam melting (EBM) and wrought Ti–6Al–4V alloys using in situ high-temperature X-ray diffraction. Int J Hydrogen Energy 2021;46(59):30423–32.
[39] Pushilina NS, Kudiiarov VN, Syrtanov MS, Kashkarov EB. Effect of the beam current during the electron-beam melting of titanium alloy Ti–6Al–4V on the structural features and phase transitions in gas-phase hydrogenation. J Surf Investig X-Ray Synchrotron Neutron Tech. 2019;13(3):429–33.
[40] Brosh E, Navi NU, Rosen BA, Eliaz N. Microvoids in electrochemically hydrogenated titanium-based alloys. Int J Hydrogen Energy 2021;46(53):27234–42.
[41] Kacenka Z, Roudnicka M, Ekrt O, Vojtech D. High susceptibility of 3D-printed Ti-6Al-4V alloy to hydrogen trapping and embrittlement. Mater Lett 2021;301:130334.
[42] Kong D, Zhao D, Zhu G, Ni X, Zhang L, Wu W, Man C, Zhou Y, Dong C, Sun B. Heat treatment effects on the hydrogen embrittlement of Ti6Al4V fabricated by laser beam powder bed fusion. Addit Manuf 2022;50:102580.
[43] Neikter M, Woracek R, Maimaitiyili T, Scheffzük C, Strobl M, Antti ML, Åkerfeldt P, Pederson R, Bjerkén C. Alpha texture variations in additive manufactured Ti-6Al-4V investigated with neutron diffraction. Addit Manuf 2018;23:225–34.
[44] Corwin WR, Lucas GE. The use of small-scale specimens for testing irradiated material: a symposium sponsored by ASTM committee E-10 on nuclear technology and applications. Albuquerque, N.M: ASTM International; 1986. 23 Sept. 1983.
[45] Bruchhausen M, Austin T, Holmström S, Altstadt E, Dymacek P, Jeffs S, Lacalle R, Lancaster R, Matocha K, Petzova J. European standard on small punch testing of metallic materials. American Society of Mechanical Engineers Digital Collection; 2017.
[46] Altstadt E, Bergner F, Das A, Houska M. Effect of anisotropic microstructure of ODS steels on small punch test results. Theor Appl Fract Mech 2019;100:191–9.
[47] Arroyo B, Álvarez JA, Gutiérrez-Solana F, Lacalle R, González P. Rate effects on the estimation of fracture toughness by small punch tests in hydrogen embrittlement. J Strain Anal Eng Des 2019;54(7–8):390–400.
[48] Eliaz N, Moshe E, Eliezer S, Eliezer D. Hydrogen effects on the spall strength and fracture characteristics of amorphous Fe-Si-B alloy at very high strain rates. Metall Mater Trans A 2000;31(4):1085–93.
[49] Snir Y, Haroush S, Dannon A, Landau A, Eliezer D, Gelbstein Y. Aging condition and trapped hydrogen effects on the mechanical behavior of a precipitation hardened martensitic stainless steel. J Alloys Compd 2019;805:509–16.
[50] García TE, Rodríguez C, Belzunce FJ, Peñuelas I, Arroyo B. Development of a methodology to study the hydrogen embrittlement of steels by means of the small punch test. Mater Sci Eng, A 2015;626:342–51.
[51] Janča A, Siegl J, Haušild P, Levỳ M. Hydrogen embrittlement of steels studied using small punch test method. Powder Metall Prog 2015;15:99–104.
[52] Arroyo B, Alvarez JA, Lacalle R, González P, Gutiérrez-Solana F. Using small punch tests in environment under static load for fracture toughness estimation in hydrogen embrittlement. IOP Conf Series: Mater Sci Eng. IOP Publishing 2017;272(1):012033.
[53] Snir Y, Haroush S, Danon A, Landau A, Gelbstein Y, Eliezer D. Metallurgical and hydrogen effects on the small punch tested mechanical properties of PH-13-8Mo stainless steel. Materials 2018;11(10):1966.
[54] Lucon E, Benzing JT, Derimow N, Hrabe N. Small punch testing to estimate the tensile and fracture properties of additively manufactured Ti-6Al-4V. J Mater Eng Perform 2021;30(7):5039–49.
[55] Illsley H, Lancaster RJ, Hurst R, Jeffs S, Baxter G. Mechanical property characterisation of electron beam melted (EBM) Ti-6Al-4V via small punch tensile testing. Key Engineering Materials. Trans Tech Publ 2017;734:51–60.

[56] Ben David R, Bitton N, Simca F, Samuha S, Fadel D, Danon A, Finkelstein Y. Non-isothermal hydrogen desorption from β-UH3: kinetics and mechanism. J Nucl Mater 2018;510:484–91.
[57] Ilyn AA, Kolachev BA, Mamonov AM. Phase and structure transformations in titanium alloys under thermohydrogenous treatment. In: Warrendale PA, Froes FH, Caplan I, editors. Titanium 92: science & technology; 1992. p. 941–7.
[58] Zhu T, Li M. Lattice variations of Ti-6Al-4V alloy with hydrogen content. Mater Char 2011;62(7):724–9.
[59] Zhao J wei, Ding H, Zhao W juan, Tian X feng, Hou H liang, Wang Y qi. Influence of hydrogenation on microstructures and microhardness of Ti6Al4V alloy. Trans Nonferrous Met Soc China 2008;18(3):506–11.
[60] Sun P, Fang ZZ, Koopman M, Paramore J, Chandran KSR, Ren Y, Lu J. An experimental study of the (Ti–6Al–4V)–xH phase diagram using in situ synchrotron XRD and TGA/DSC techniques. Acta Mater 2015;84:29–41.
[61] Navi NU, Rosen BA, Sabatani E, Tenenbaum J, Tiferet E, Eliaz N. Thermal decomposition of titanium hydrides in electrochemically hydrogenated electron beam melting (EBM) and wrought Ti–6Al–4V alloys using in situ high-temperature X-Ray diffraction. Int J Hydrogen Energy 2021;46(59):30423–32.
[62] Haroush S, Moreno D, Silverman I, Turgeman A, Shneck R, Gelbstein Y. The mechanical behavior of HAVAR foils using the small punch technique. Materials 2017;10(5):491.
[63] ASTM F2924-14 - Standard Specification for Additive Manufacturing Titanium-6 Aluminum-4 Vanadium with Powder Bed Fusion Available from, https://webstore.ansi.org/standards/astm/astmf292414.
[64] Razavi SMJ, Berto F. Directed energy deposition versus wrought Ti-6Al-4V: a comparison of microstructure, fatigue behavior, and notch sensitivity. Adv Eng Mater 2019;21(8):1900220.
[65] Ganor YI, Tiferet E, Vogel SC, Brown DW, Chonin M, Pesach A, Hajaj A, Garkun A, Samuha S, Shneck RZ, Yeheskel O. Tailoring microstructure and mechanical properties of additively-manufactured Ti6Al4V using post processing. Materials 2021;14(3):658.
[66] Rafi HK, Karthik NV, Gong H, Starr TL, Stucker BE. Microstructures and mechanical properties of Ti6Al4V parts fabricated by selective laser melting and electron beam melting. J Mater Eng Perform 2013;22(12):3872–83.
[67] Zhou L, Liu HJ. Effect of hydrogenation on microstructure and mechanical properties of Ti-6Al-4V titanium alloy. Adv Mater Res 2013;750:596–602.
[68] Gu J, Hardie D. Effect of hydrogen on structure and slow strain rate embrittlement of mill annealed Ti6Al4V. Mater Sci Technol 1996;12(10):802–7.